Materials and Design 55 (2014) 482–491

Contents lists available at ScienceDirect

Materials and Design

journal homepage: www.elsevier.com/locate/matdes

Thermal behavior and densification mechanism during selective laser melting of copper matrix composites: Simulation and experiments

Donghua Dai, Dongdong Gu *

College of Materials Science and Technology, Nanjing University of Aeronautics and Astronautics (NUAA), Yudao Street 29, 210016 Nanjing, PR China

ARTICLE INFO

Article history:
Received 11 August 2013
Accepted 1 October 2013
Available online 14 October 2013

Keywords:
Numerical simulation
Additive manufacturing
Selective laser melting
Metal matrix composites
Marangoni flow

ABSTRACT

Simulation of temperature distribution and densification process of selective laser melting (SLM) WC/Cu composite powder system has been performed, using a finite volume method (FVM). The transition from powder to solid, the surface tension induced by temperature gradient, and the movement of laser beam power with a Gaussian energy distribution are taken into account in the physical model. The effect of the applied linear energy density (LED) on the temperature distribution, melt pool dimensions, behaviors of gaseous bubbles and resultant densification activity has been investigated. It shows that the temperature distribution is asymmetric with respect to the laser beam scanning area. The center of the melt pool does not locate at the center of the laser beam but slightly shifts towards the side of the decreasing *X*-axis. The dimensions of the melt pool are in sizes of hundreds of micrometers and increase with the applied LED. For an optimized LED of 17.5 kJ/m, an enhanced efficiency of gas removal from the melt pool is realized, and the maximum relative density of laser processed powder reaches 96%. As the applied LED surpasses 20 kJ/m, Marangoni flow tends to retain the entrapped gas bubbles. The flow pattern has a tendency to deposit the gas bubbles at the melt pool bottom or to agglomerate gas bubbles by the rotating flow in the melt pool, resulting in a higher porosity in laser processed powder. The relative density and corresponding pore size and morphology are experimentally acquired, which are in a good agreement with the results predicted by simulation.

1. Introduction

In recent years, there have been a lot of focuses on the fabrication of copper matrix composites (CMCs) due to their excellent electrical properties, thermal conductivity and good resistance to oxidation [1–3]. WC, due to its high hardness, good wear resistance and high elastic modulus, is regarded as a good reinforcement material for Cu [1]. Thus WC/Cu composites are the suitable candidates for a typical use in high-voltage electrical applications [2]. Generally, the WC/Cu parts are fabricated using common casting and powder metallurgy (PM) methods, which need expensive and dedicated tools such as mould or dies [4,5]. However, the requirement of processing temperatures being significantly above the melting point of copper (1390 K) is the shortcoming of the conventional processes for WC/Cu composites [2], which may result in the abnormal grain growth and accordingly produces the poor mechanical properties. Therefore, it seems that the conventional processing approaches have the limited capacity to meet the high industrial requirements for CMCs parts. Meanwhile, parts with complex geometrical shapes cannot be fabricated easily via the conventional methods. Therefore, both demands for obtaining complex features and high comprehensive mechanical properties are expected to be satisfied by using other novel processing technique.

Selective laser melting (SLM), as a newly developed additive manufacturing (AM) technique, enables the quick fabrication of three-dimensional parts with any complex shapes directly from metal powder [6–10]. The SLM process creates parts in a layer-by-layer fashion by selectively melting thin layers of loose powder with a high energy laser beam [11,12]. This technique competes effectively with other conventional manufacturing processes as the part configuration is complex and the production run is not large. Although recent advances in SLM have considerably promoted this technology, this method essentially relies on empirical, experimental knowledge and still lacks a strong theoretical basis [13]. This may be attributed to the complex metallurgical process of SLM, which exhibits multiple modes of heat, mass and momentum transfer [14,15]. One of the uncontrollable defects of SLM process is high porosity, which is detrimental to the final mechanical properties of SLM parts [16,17]. Many investigations, aiming to obtain a high densification level for SLM parts, have been reported. Zhang et al. [18] studied the effects of processing parameters on properties of SLM Mg–9%Al powder mixture. It was found that porosity of samples was highly dependent on the energy density,

* Corresponding author. Tel./fax: +86 25 52112626.
E-mail address: dongdonggu@nuaa.edu.cn (D. Gu).

0261-3069/$ - see front matter © 2013 Elsevier Ltd. All rights reserved.
http://dx.doi.org/10.1016/j.matdes.2013.10.006

Nomenclature

A	laser absorptivity of the powder
C_p	specific heat at constant pressure, J/(kg K)
D_p	average diameter of the powder particles, m
E	total energy, J
$\vec{F}$	force vector
g	gravitational acceleration, m/s^2
h	sensible enthalpy, J/kg
h_c	convective heat transfer coefficient, W/(m^2 K)
h_{ref}	reference enthalpy, J/kg
H	enthalpy of the material, J/kg
ΔH	latent heat of the phase change, J/kg
p	pressure, Pa
P	laser power, W
S_h	source item of the radiation and any other volumetric heat sources
S_H	source item of the energy conservation equation
S_x, S_y, S_z	source item of the momentum conservation equation
S_{α_i}	mass source for each phase
t	time, s
T	temperature, K
T_∞	ambient temperature, K
T_p	temperature of the powder particles, K
T_{ref}	reference temperature, K
v_b	velocity of the gaseous bubble, m/s
$\vec{v}$	overall velocity vector, m/s
u, v, w	velocity magnitude, m/s
x, y, z	coordinates, m
α	volume fraction of the gas phase
α_i	volume fraction of each phase
γ	surface tension, N/m
ε	radiation emissivity
κ	thermal conductivity of the powder bed, W/(m K)
κ_s	thermal conductivity of the solid, W/(m K)
κ_{eff}	effective thermal conductivity of liquid–solid–gas multi-phases, W/(m K)
κ_f	thermal conductivity of the fluid, W/(m K)
κ_r	thermal conductivity due to the radiation among particles, W/(m K)
μ	dynamic viscosity, Pa s
ρ	density, kg/m^3
ρ_i	density of each phase, kg/m^3
σ_e	Stefan–Boltzmann constant
ω	radius of the Gaussian laser beam, m

and eventually the densification mechanism during SLM was established by the authors. Hazlehurst and his coworkers [19] focused on the design and fabrication of cobalt chrome molybdenum cellular structures with different porosities via SLM. It was shown that mechanical properties were significantly influenced by the volumetric porosity. Saha et al. [20] investigated the crack density and wear performance of Al-based metal matrix composite fabricated by direct metal laser sintering (DMLS) AM process. The size and volume fraction of SiC reinforcing particles were varied to analyze the density and wear behavior of laser processed composites. Ferrar et al. [21] studied the effect of inert gas flow during the SLM process on the mechanical performance of SLM parts, in order to enable the production of desired components with a greater reproducibility.

Although the porosity rate can be decreased by optimizing laser parameters and improving scanning strategy during SLM, the inner porosity normally cannot be completely eliminated [22,23]. To date, little work has been focused on the effects of gas phase in the starting powder system on the densification behavior of powder under various SLM processing conditions. Furthermore, the unique metallurgical process of SLM, e.g. the presence of significant Marangoni effect and the super high undercooling degree, significantly impedes the systematic investigation of the densification activity of the melt pool during SLM process. Therefore, it is of great importance and necessity to find a feasible method to quantitatively reveal the densification behavior of SLM-processed powder and to predict the undesired porosity appeared in the finally solidified melt.

In this work, the numerical simulation regarding the influence of the linear energy density (LED) of laser beam on the melt pool dynamics and densification mechanisms during SLM of WC/Cu powder system was presented, using Fluent 6.3.26 commercial finite volume method (FVM) software. The fluid flow driven by surface tension gradient and gravity forces was considered in the physical model and the temperature distribution, melt pool dimensions, behaviors of bubbles and Marangoni convection were simulated. Furthermore, the relative densities of SLM parts obtained by numerical simulation were compared with those acquired via experiments, in order to testify the accuracy of the developed simulation model and obtain reasonable SLM processing conditions to produce high density WC/Cu parts.

2. Model descriptions

Fluent 6.3.26 software, which enables simulation of processes with molten metal flow and behavior of the gaseous bubbles, is introduced to simulate SLM process. To simplify the problem, the following assumptions are made in this study: (1) The melt in the molten pool is assumed to be laminar and incompressible homogeneous Newtonian fluid; (2) Except thermal conductivity, surface tension and viscosity, some other thermal physical constants are considered to be temperature independent; and (3) The metal vaporization is ignored.

2.1. Physical model

The schematic of SLM physical model is depicted in Fig. 1. In simulation the laser beam is defined as a heat flux, $q_{(x,y,z,t)}$, with a Gaussian power distribution as an incoming heat source, which moves at a constant rate along the X-axis. The geometry of this source is assumed by the absorption phenomenon in the skin layer.

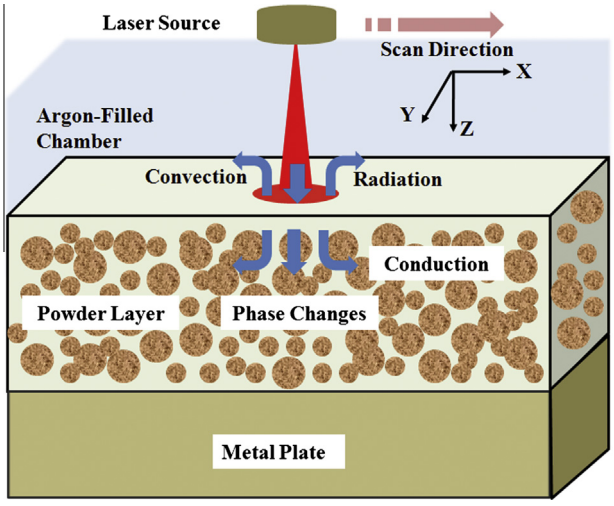

Fig. 1. Schematic of SLM physical model.

The laser radiation can penetrate into the powder layer but only up to a certain distance from the surface, which is called "penetration depth". The heat losses from the six surfaces of the model are assumed to result from the natural convection and radiation. The powder system consists of WC, Cu and gas with the volume ratio of 15:55:30. The three-dimensions of the numerical model are $3 \times 1 \times 0.6$ mm. The initial temperature of the powder layer, T_i, is treated as the room temperature. As the laser beam interacts with the powder, a molten pool is formed under the laser beam and the melt infiltrates into the powder layer driven by the capillary and gravitational forces.

2.2. Governing equations

Based on the mass equation, momentum equation and energy equation, the governing equations in the Cartesian coordinate system are summarized as follows [24].

2.2.1. Mass conservation equation

$$\frac{\partial \rho}{\partial t}+\frac{\partial(\rho u)}{\partial x}+\frac{\partial(\rho v)}{\partial y}+\frac{\partial(\rho w)}{\partial z}=0 \tag{1}$$

2.2.2. Momentum conservation equation

(1) Momentum conservation equation in the X direction:

$$\begin{aligned}&\frac{\partial(\rho u)}{\partial t}+\frac{\partial(\rho u u)}{\partial x}+\frac{\partial(\rho u v)}{\partial y}+\frac{\partial(\rho u w)}{\partial z}\\&=-\frac{\partial p}{\partial x}+\frac{\partial}{\partial x}\left[\mu\left(2\frac{\partial u}{\partial x}-\frac{2}{3}\nabla\cdot\vec{v}\right)\right]+\frac{\partial}{\partial y}\left[\mu\left(\frac{\partial u}{\partial y}+\frac{\partial v}{\partial x}\right)\right]\\&+\frac{\partial}{\partial z}\left[\mu\left(\frac{\partial u}{\partial z}+\frac{\partial w}{\partial x}\right)\right]+S_x\end{aligned} \tag{2}$$

(2) Momentum conservation equation in the Y direction:

$$\begin{aligned}&\frac{\partial(\rho v)}{\partial t}+\frac{\partial(\rho u v)}{\partial x}+\frac{\partial(\rho v v)}{\partial y}+\frac{\partial(\rho v w)}{\partial z}\\&=-\frac{\partial p}{\partial y}+\frac{\partial}{\partial y}\left[\mu\left(2\frac{\partial v}{\partial y}-\frac{2}{3}\nabla\cdot\vec{v}\right)\right]\\&+\frac{\partial}{\partial x}\left[\mu\left(\frac{\partial u}{\partial y}+\frac{\partial v}{\partial x}\right)\right]+\frac{\partial}{\partial z}\left[\mu\left(\frac{\partial v}{\partial z}+\frac{\partial w}{\partial y}\right)\right]+S_y\end{aligned} \tag{3}$$

(3) Momentum conservation equation in the Z direction:

$$\begin{aligned}&\frac{\partial(\rho w)}{\partial t}+\frac{\partial(\rho u w)}{\partial x}+\frac{\partial(\rho v w)}{\partial y}+\frac{\partial(\rho w w)}{\partial z}\\&=-\frac{\partial p}{\partial z}+\frac{\partial}{\partial z}\left[\mu\left(2\frac{\partial w}{\partial z}-\frac{2}{3}\nabla\cdot\vec{v}\right)\right]\\&+\frac{\partial}{\partial x}\left[\mu\left(\frac{\partial w}{\partial x}+\frac{\partial u}{\partial z}\right)\right]+\frac{\partial}{\partial y}\left[\mu\left(\frac{\partial w}{\partial y}+\frac{\partial v}{\partial z}\right)\right]+S_z\end{aligned} \tag{4}$$

2.2.3. Energy conservation equation

$$\begin{aligned}&\frac{\partial(\rho T)}{\partial t}+\frac{\partial(\rho u T)}{\partial x}+\frac{\partial(\rho v T)}{\partial y}+\frac{\partial(\rho w T)}{\partial z}\\&=\frac{\partial}{\partial x}\left(\kappa\frac{\partial T}{\partial x}\right)+\frac{\partial}{\partial y}\left(\kappa\frac{\partial T}{\partial y}\right)+\frac{\partial}{\partial z}\left(\kappa\frac{\partial T}{\partial z}\right)+S_H\end{aligned} \tag{5}$$

where ρ, κ, μ and p are the density, thermal conductivity, viscosity and pressure, respectively. S_x, S_y and S_z represent the source item of the momentum conservation equation in the X, Y and Z direction, respectively. S_H is the source item of the energy conservation equation in the X, Y and Z direction and can be defined by:

$$S_H=-\left(\frac{\partial}{\partial t}(\rho\Delta H)+\frac{\partial}{\partial x}(\rho u\Delta H)+\frac{\partial}{\partial y}(\rho v\Delta H)+\frac{\partial}{\partial z}(\rho w\Delta H)\right) \tag{6}$$

where ΔH is the latent heat of phase change. The enthalpy of the material is computed as the sum of the sensible enthalpy, h, and the latent heat, ΔH. The enthalpy of the material, H, can be defined by:

$$H=h+\Delta H \tag{7}$$

where $h=h_{ref}+\int_{T_{ref}}^{T}C_p dT$.

2.2.4. Equations of volume of fluid (VOF) model

The volume fraction equation for the i phase is [25]:

$$\frac{\partial \alpha_i}{\partial t}+\vec{v}\cdot\nabla\alpha_i=\frac{S_{\alpha_i}}{\rho_i} \tag{8}$$

where $\sum_{i=1}^{n}\alpha_i=1$, n represents the phase number.

A single momentum equation is solved throughout the domain, and the resulting velocity field is shared among the phases [25]:

$$\frac{\partial}{\partial t}(\rho\vec{v})+\nabla(\rho\vec{v}\vec{v})=-\nabla p+\nabla[\mu(\nabla\vec{v}+\nabla\vec{v}^T)]+\rho g+\vec{F} \tag{9}$$

The density ρ and dynamic viscosity μ in the equation are dependent on the volume fraction of all phases:

$$\rho=\sum\alpha_i\rho_i \tag{10}$$

$$\mu=\sum\alpha_i\mu_i \tag{11}$$

The transport of mass and momentum for the laminar and incompressible homogeneous Newtonian fluid is expressed in Eqs. (1)–(4). The governing equations are discretized on a staggered Cartesian grid system, including local mesh refinements at regions with larger gradients. The initially gaseous bubbles are dispersed in the physical domain with a zero velocity, which will be tracked when they accelerate under the effect of the Marangoni flow. The average bubble velocity located in a specific region of the melt pool is obtained using the summation over all cells [26]:

$$v_{\text{average}}=\frac{\sum v_b\alpha}{\sum\alpha} \tag{12}$$

where α is the volume fraction of the gas phase during the numerical simulation and v_b is the velocity of the gaseous bubbles.

The energy equation is also shared among the phases [25]:

$$\frac{\partial}{\partial t}(\rho E)+\nabla[\vec{v}(\rho E)+\rho]=\nabla(\kappa_{eff}\nabla T)+S_h \tag{13}$$

The VOF model treats energy, E, and temperature, T, as mass-averaged variables:

$$E=\frac{\sum_{i=1}^{n}\alpha_i\rho_i E_i}{\sum_{i=1}^{n}\alpha_i\rho_i} \tag{14}$$

where E_i for each phase is based on the specific heat of that phase and the shared temperature. The effective thermal conductivity, κ_{eff}, is also shared by the phases. The source term, S_h, contains contributions from radiation as well as any other volumetric heat sources.

2.3. Boundary conditions

The boundary condition at the top surface ($Z=0$) is given by [27]:

$$-\kappa\left(\frac{\partial T}{\partial z}\right)_{z=0} = \frac{2AP}{\pi\omega^2}\exp\left(-\frac{2r^2}{\omega^2}\right) - h_c(T-T_\infty) - \sigma_e\varepsilon(T^4-T_\infty^4) \tag{15}$$

where ω is the radius of the Gaussian laser beam at which the heat flux value is e^{-2} times of that of the laser beam center, A is the absorptance of the powder system, r is the distance of a point on the surface of the powder bed measured from the laser beam center at time t, T_∞ is the ambient temperature, h_c is the heat transfer coefficient of natural thermal convection, σ_e is the Stefan–Boltzmann constant and ε is the emissivity. To simulate the Marangoni flow due to temperature gradient at the top surface, the surface tension is given by [28]:

$$-\mu\frac{\partial \mu}{\partial z} = \frac{\partial \gamma}{\partial T}\frac{\partial T}{\partial x} \tag{16}$$

$$-\mu\frac{\partial \mu}{\partial z} = \frac{\partial \gamma}{\partial T}\frac{\partial T}{\partial y} \tag{17}$$

The temperature on the lateral surfaces is defined as the ambient temperature and the mechanism of the heat loss is assumed to be the radiation, with the mathematical expression shown by the last item of Eq. (15). The bottom of the powder layer is connected to the metal substrate with larger heat conductivity in comparison with the gas. As a result heat loss through interface between powder layer and substrate is faster.

2.4. Physical properties

Assuming that the particles are spheres and there is no flattening of contact surfaces, the effective thermal conductivity of the powder bed, κ, is estimated by [29]:

$$\frac{\kappa}{\kappa_f} = (1-\sqrt{1-\alpha})\left(1+\frac{\alpha\kappa_r}{\kappa_f}\right) + \sqrt{1-\alpha}\left[\frac{2}{1-\frac{\kappa_f}{\kappa_s}}\left(\frac{1}{1-\frac{\kappa_f}{\kappa_s}}\ln\left(\frac{\kappa_s}{\kappa_f}\right)-1\right)+\frac{\kappa_r}{\kappa_f}\right] \tag{18}$$

where α is the fractional porosity of the powder bed, κ_f is the thermal conductivity of the fluid surrounding the powder particles, κ_s is the thermal conductivity of the solid, κ_r is the thermal conductivity in the powder bed due to the radiation among particles, which is further defined by:

$$\kappa_r = 4B\sigma_e T_p^3 D_p \tag{19}$$

where σ_e is the Stefan–Boltzmann constant, D_p is the average diameter of the powder particles, T_p is the temperature of the powder particles, and B is a view factor which is approximately taken as 1/3.

The laser absorptivity of the powder system is determined by both the physical properties of WC and Cu and the volume fraction of each phase, as defined by:

$$A = \sum \alpha_i A_i \tag{20}$$

where $\sum_{i=1}^{n}\alpha_i = 1$, n represents the phase number, A_i is the laser absorptivity of i phase in the calculated system.

2.5. Numerical simulation

The simulation is carried out using the FLUENT commercial finite volume method package (version 6.3.26) to simulate the thermal behavior, velocity field and the gaseous bubbles behavior. The thermal physical properties of WC and Cu components are depicted in Fig. 2 [30,31]. The as-used material properties and SLM processing parameters are shown in Table 1.

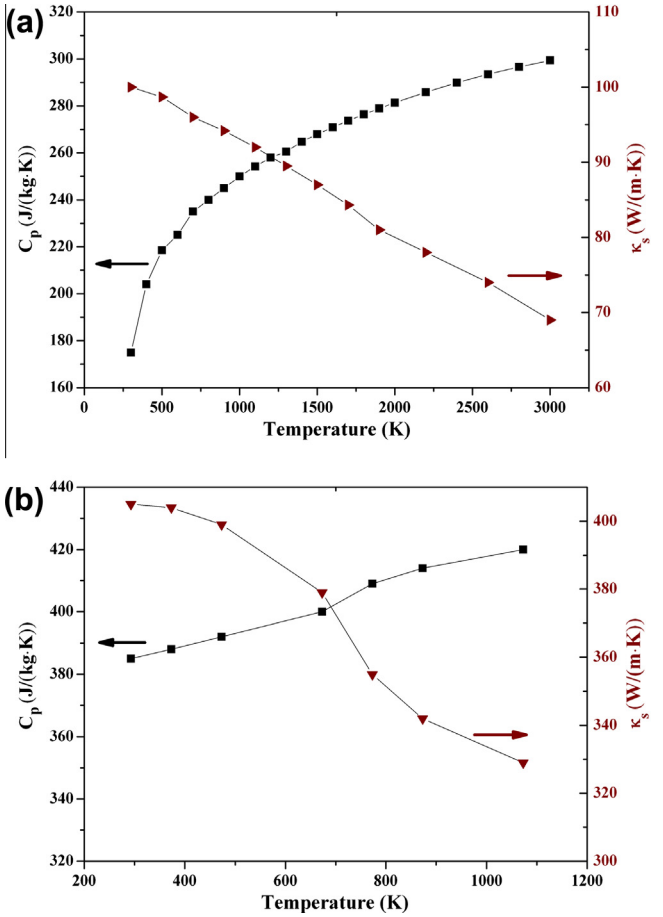

Fig. 2. Thermal physical properties of tungsten carbide (a) and copper (b).

Table 1
The as-used material properties and SLM processing conditions.

Parameter	Value
Ambient temperature, T_∞	300 K
Convective heat transfer coefficient, h_c	80 W/(m^2 K)
The Stefan–Boltzmann constant, σ_e	5.67×10^{-8} W/(m^2 K^4)
Radiation emissivity, ε	0.36
Laser absorptivity of the Cu powder	0.4
Laser absorptivity of the WC powder	0.6
Powder layer thickness, l_p	250 μm
Laser power, P	600–900 W
Radius of laser beam, ω	0.3 mm

3. Experimental procedures

3.1. Powder materials

Electrolytic 99% purity Cu powder with a dendrite shape and an average particle size of 15 μm, and WC powder with an equiaxed shape and a mean particle size of 0.6 μm are used in this study. The two components are mixed according to the ratio mentioned in the simulation.

3.2. Processing and characterization

The SLM apparatus used in this experiment mainly consists of a continuous wave Gaussian CO_2 laser with a maximum power of 2000 W and a spot size of 300 μm (supplier: Rofin-Sinar Laser GmbH), an automatic powder layering apparatus, an inert argon

gas protection system, and a computer system for process control. Details of the SLM process are summarized in [32,33]. The processing conditions investigated are the same as the data in the numerical simulation. The densities of SLM-processed specimens were determined based on the Archimedes principle. Samples for metallographic examinations were cut, ground and polished according to standard procedures. Microstructures were characterized using an Olympus PMG3 optical microscopy (OM).

4. Results and discussion

4.1. Temperature distribution

Fig. 3a shows the temperature distribution along X-axis on the top surface ($Y = 0$) with different LEDs during laser irradiation. The profiles of the temperature distribution depict that there is an enhancement in temperature with an increase in LED. For a relatively lower LED of 15 kJ/m, the maximum temperature is merely 1420 K, which is close to the melting point of Cu (1390 K). Under this condition, the inadequate energy input may give rise to poor metallurgical bonding ability between the currently processed layer and the previously processed one [34]. Whereas, at a considerably elevated LED of 22.5 kJ/m, the maximum temperature in the melt pool is as high as 1834.8 K. In this situation, the melt tends to splash, caused by a high capillary instability of the melt due to the overheating of local regions. The "balling" effect, which is a typical metallurgical defect of SLM process, is likely to occur in this instance, thereby decreasing the densification level of the final parts [35]. Meanwhile, the temperature gradient during this fabrication process is the highest with the value of 3.9×10^5 K/m, which accordingly contributes to the formation of a significantly high stress field. Consequently, the thermal cracks tend to be formed in the SLM-processed parts due to the release of the stresses [33,34,36]. In other two cases, the maximum temperatures are 1588 K and 1695 K, respectively, at the LED of 17.5 kJ/m and 20 kJ/m. From Fig. 3b, it is worth noting that the melt pool is asymmetric with respect to the laser beam area. The center of the melt

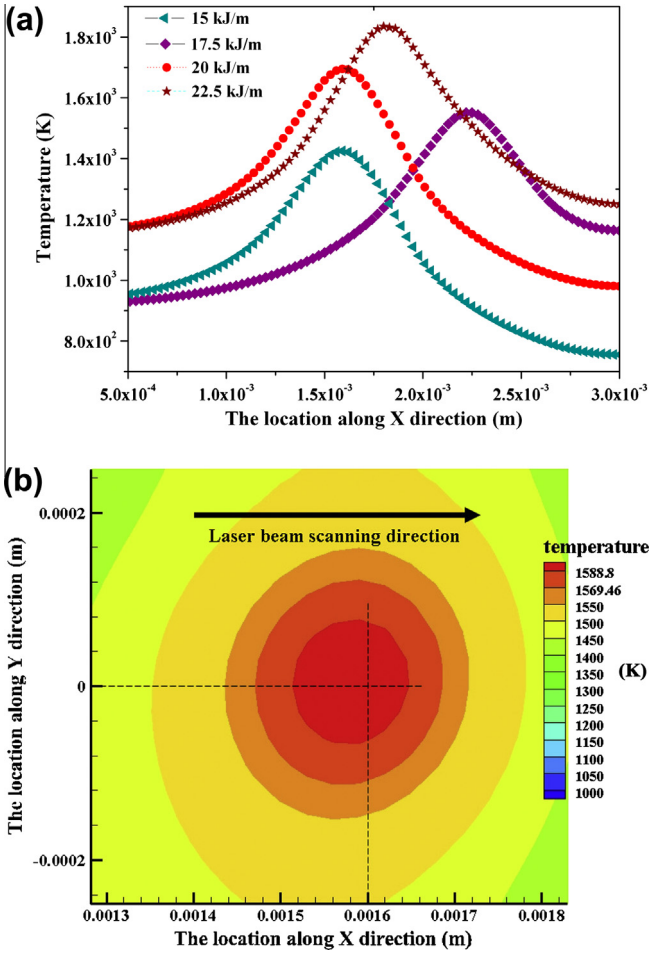

Fig. 3. Temperature distribution at different linear energy densities (LEDs) on the scanning path along X-axis at $Y = 0$ and $Z = 0$ (a) and the temperature contour plot at the LED of 17.5 kJ/m (b).

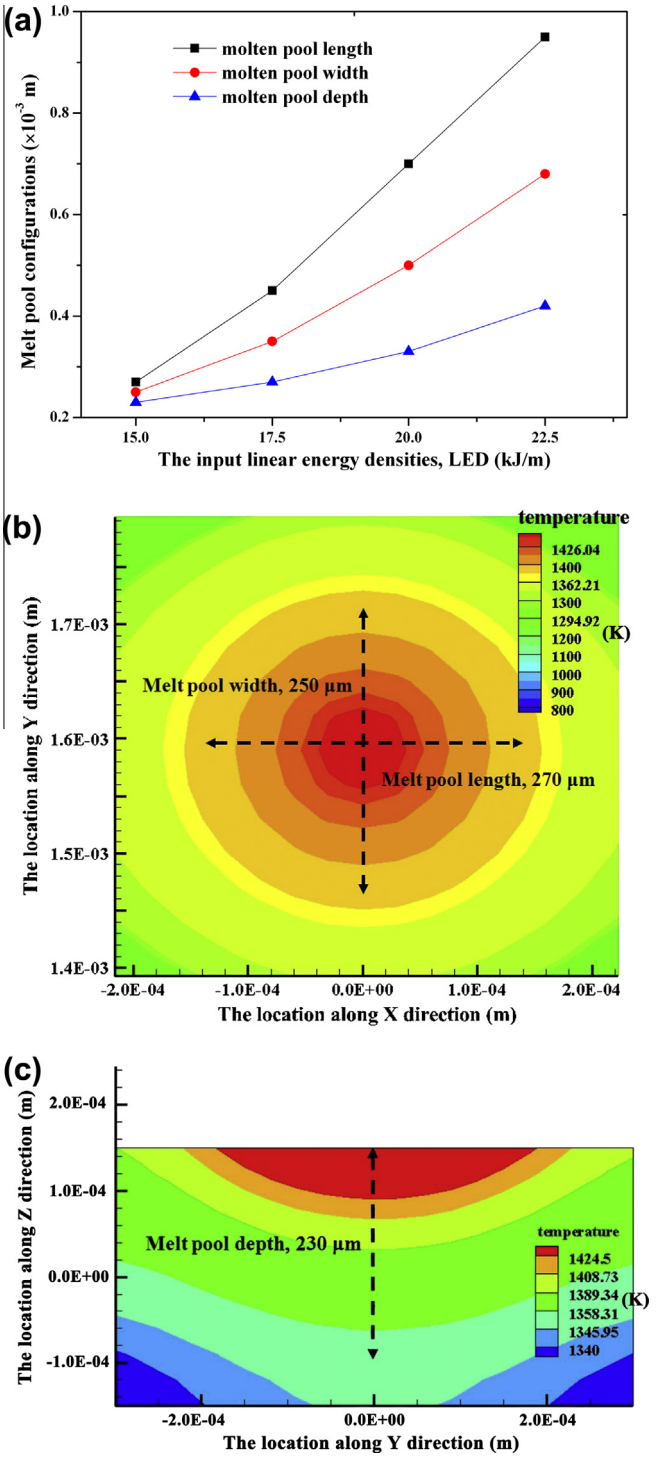

Fig. 4. The three-dimensions of melt pool at various LEDs (a); The melt pool length and width (b) and melt pool depth (c) at the LED of 15 kJ/m.

pool does not locate at the center of the laser beam (X = 0.0016 m; Y = 0), but slightly shifts towards the side of the decreasing X-axis (Fig. 3b). This phenomenon is attributed to the combination of thermal accumulation effect and the change of thermal conductivity owing to the transition from powder to solid [37]. The as-irradiated regions located behind the scanning laser beam are getting heated frequently. Therefore, the center of melt pool along X-axis is observed to be slightly towards the previous scanned zones (i.e., the decreasing X-axis).

4.2. Melt pool dimensions

Fig. 4 depicts that the melt pool length (along X-axis), width (along Y-axis) and depth (along Z-axis) are proportional to the applied LED. The three-dimensions of the melt pool are extracted from the isotherms that are above the melting point of Cu. It can be found that the melt pool dimensions change with applied LEDs and are in sizes of hundreds of micrometers. All of the simulated melt pool length, width and depth increase with the enhancement of LEDs, whereas there is a significant distinction in the increment rate. Generally, the observation demonstrates that an increase in LED leads to an increase in the melt pool dimensions. Melt pool length at LED of 15 kJ/m is 270 μm and at LED of 22.5 kJ/m is 950 μm, which indicates that the melt pool length has approximately a linear relationship with the input LEDs. The same rule is identified for the melt pool width and the width values at LEDs of 15 kJ/m and 22.5 kJ/m are 250 μm and 680 μm, respectively. Moreover, for a fixed LED (e.g. for LED of 17.5 kJ/m), the melt pool length (~450 μm) is larger than the melt pool width (~350 μm). This phenomenon can be explained that the laser beam is moving along X-axis and the regions along the laser path are repeatedly heated. Therefore, for the points at X-axis and Y-axis that have the same distance from the center of the melt pool, the temperature is higher at X-axis than that at Y-axis (Fig. 4b). On the other hand, the laser penetration depth must be higher than the powder layer thickness, in order to ensure that the neighboring layers are well bonded [38]. The melt pool depth at LED of 15 kJ/m is 230 μm (Fig. 4c), which is less than the starting powder layer thickness (250 μm). It indicates that the as-formed molten tracks are not bonded efficiently with the previously processed layers, due to the limited laser penetration depth. As LED increases to 17.5 kJ/m, the melt pool depth is 270 μm. On further increasing the LED from 20 kJ/m to 22.5 kJ/m, the melt pool depth increases from 330 μm to 420 μm. It is accordingly concluded that an enhancement in LED leads to a deeper laser penetration depth. As relative to the melt pool length and width, the increase rate of the melt pool depth with the applied LED is much slighter (Fig. 4a).

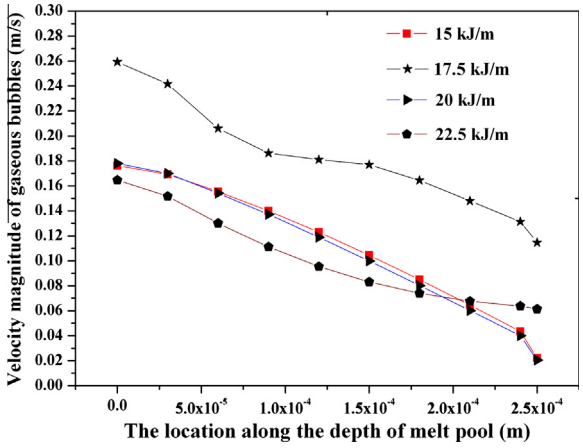

Fig. 5. The velocity magnitude of gaseous bubbles floating up to the melt pool surface at different LEDs.

4.3. Motion of gaseous bubbles

In order to investigate the influence of applied LEDs on the motion of gaseous bubbles, the velocity magnitude of gaseous bubbles from the bottom region to the top surface is studied, as depicted in Fig. 5. It is clear that the speeds of gaseous bubbles continuously accelerate from the bottom to the top surface. For a relatively low LED of 15 kJ/m, the obtained speed at the depth of 250 μm is 0.02 m/s, while at the top surface the speed increases to 0.18 m/s. As LED increases to 17.5 kJ/m, the speeds of gaseous bubbles at the depth of 250 μm and top surface are 0.12 m/s and 0.26 m/s, respectively. Under this condition, it implies that gaseous bubbles have a tendency to rise faster and escape from the melt pool. However, for a relatively high LED of 20 kJ/m, the speeds of gaseous bubbles decrease sharply and are almost similar as the speeds obtained at LED of 15 kJ/m. As LED further increases to 22.5 kJ/m, the curve of the speeds of gaseous bubbles along the melt pool

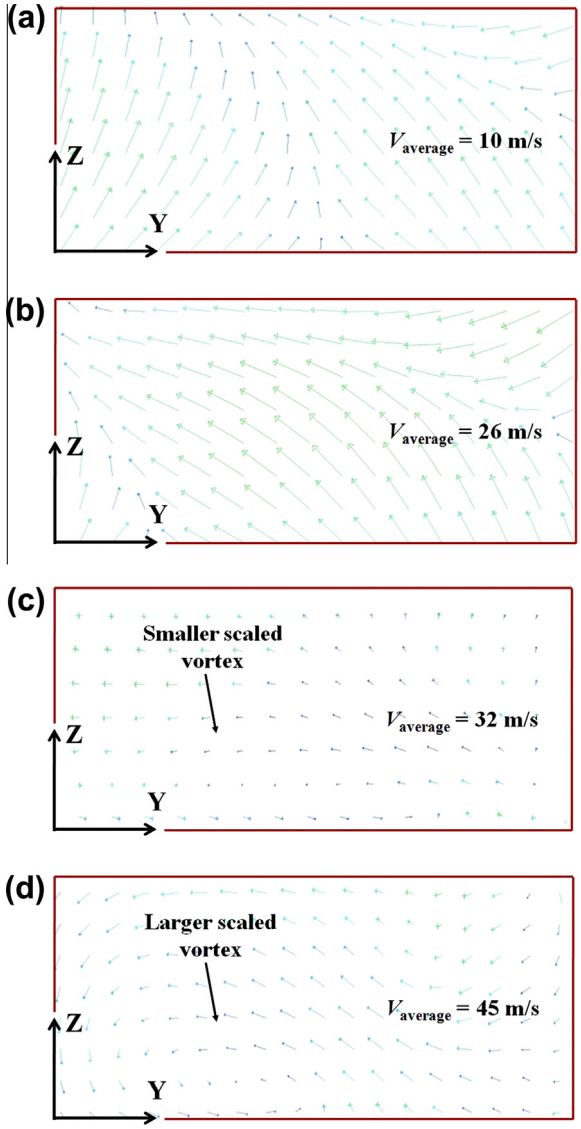

Fig. 6. The velocity vector plots of convection flow in the melt pool at various LEDs (cross-sectional view): (a) LED = 15 kJ/m, (b) LED = 17.5 kJ/m, (c) LED = 20 kJ/m, and (d) LED = 22.5 kJ/m.

depth becomes more complicated. Along the melt pool depth ranging from 212 μm to 250 μm, the speeds are higher than those obtained at LEDs of 15 kJ/m and 20 kJ/m, but are lower than those obtained at LED of 17.5 kJ/m. Moreover, along the distance from the top surface to the melt pool depth of 180 μm, the speeds of gaseous bubbles are lowest in this instance.

During SLM process, the thermocapillary flow (Marangoni convection) induced by surface tension variations along free surface is an important phenomenon [39], because it plays a crucial role in determining the behaviors of gaseous bubbles [40,41]. Fig. 6 displays the velocity vector plots of convection flow under various LEDs. It is obvious that the intensity of the fluid flow increases with the enhancement of input LEDs. For LEDs of 15 kJ/m and 17.5 kJ/m, the high-temperature melt near the central region floats up to the free surface with the average velocity of 10 m/s and 26 m/s, respectively (Fig. 6a and b). Interestingly, as LED increases to 20 kJ/m, it is apparent to find a smaller scaled vortex in the bottom section of the melt pool (Fig. 6c). As LED further increases to 22.5 kJ/m, a larger scaled vortex is found with the fluid flow velocity of 45 m/s (Fig. 6d). The influence of the fluid flow under various LEDs on the bubbles movement is depicted in Fig. 7. For a relatively low LED of 15 kJ/m, most of the bubbles are entrapped below the surface of the melt pool due to the lower speeds obtained by the bubbles (Fig. 7a). As LED increases to 17.5 kJ/m, a majority of bubbles escape the melt pool easily with higher movement speeds (Figs. 5 and 7b). Therefore, a more significant densification response of the melt pool is expected under this processing condition. However, for a relatively high LED of 20 kJ/m, although the bubbles in the upper section of the melt pool still have the capability to escape from the pool, the presence of the rotational pattern of the flow vortex (Fig. 6c) tends to entrap the gaseous bubbles at the bottom of the melt pool (Fig. 7c). As LED further increases to 22.5 kJ/m, the gaseous bubbles are entrapped easily by the larger scaled vortex (Fig. 7d) and the bubbles tend to be transported to the centre of the rotating flow due to the lower density of a gas/melt multiphase mixture. Meanwhile, the centrifugal forces act on the rotating flow, resulting in the formation of severe agglomeration of bubbles in the middle section of melt pool. It is accordingly concluded that as the dynamics of fluid flow increase with the elevated LEDs, there is an enhanced possibility that the gas in the starting powder layer become trapped and dragged in the melt pool, thereby producing the residual porosity in the finally solidified parts.

4.4. Densification behavior

Since SLM is a multi-line based scanning process in each processing layer, the characteristics of single scanning track have an apparent effect on the resultant multi-line and multi-layer forming conditions. In this simulation of the densification behavior during SLM process, the starting powder system is irradiated by the laser beam. A melt pool will be produced and resultant Marangoni convection tends to be formed due to the surface tension [42]. Under the effect of different Marangoni flow profiles, the gaseous bubbles have a tendency to show various activities in the melt pool (Figs. 6 and 7). The densification behavior during the SLM process, as investigated in this

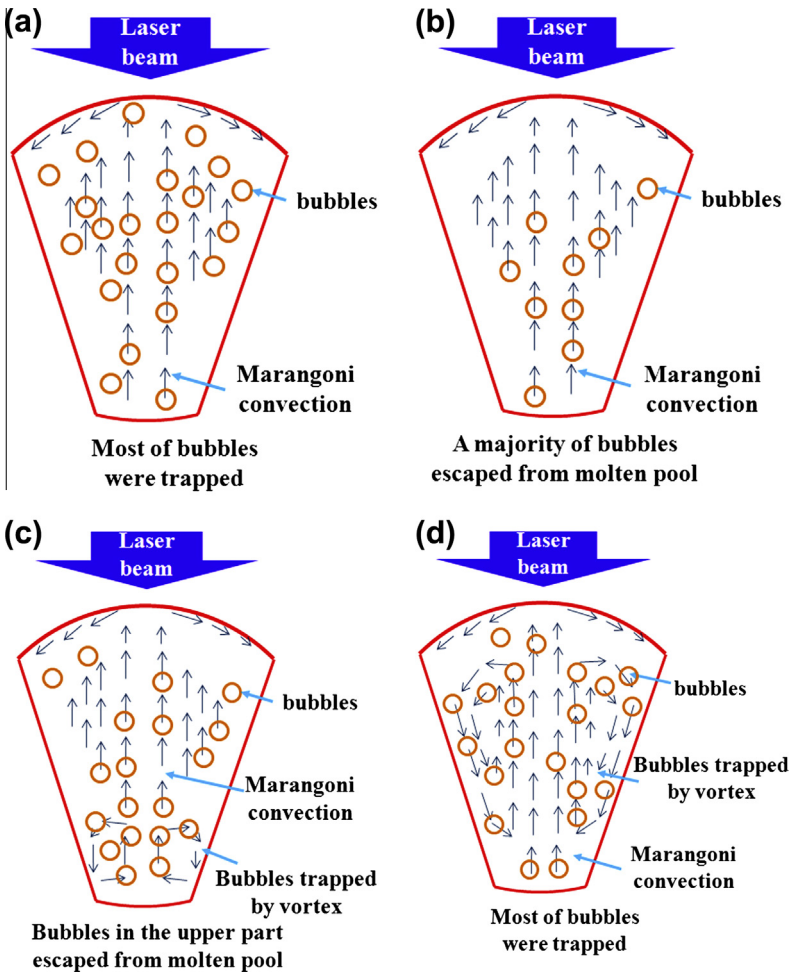

Fig. 7. The schematics of gaseous bubbles movement in the melt pool on increasing LEDs: (a) LED = 15 kJ/m, (b) LED = 17.5 kJ/m, (c) LED = 20 kJ/m, and (d) LED = 22.5 kJ/m.

established physical model, is identified by the combined effect of the Marangoni convection in the melt pool and the motion of the gaseous bubbles. Namely, as the gas bubbles escape from the melt pool, the volume fraction of the other phases in the solidified part will be accordingly enhanced. Fig. 8 shows the contour plots of relative densities in the longitudinal sections of single scan tracks under different LEDs. The areas within the melt pool of the similar density can be identified in the similar shades. This method of data representation makes it easier to identify the densification rate with respect to position within the melt pool. It is noted that the input LED has a significant effect on the distribution of the density (i.e., the densification behavior). For a relatively low LED of 15 kJ/m, the relative density is about 93% from the free surface of melt pool to the pool depth of 170 μm. While for the pool depth over 170 μm, the relative density is approximately 90% (Fig. 8a). When LED increases to 17.5 kJ/m, the mean porosity is reduced, due to the increased efficiency of gas removal from the melt pool (Figs. 5 and 7b). The maximum relative density is 96% and from the free surface to the depth of 200 μm the relative density is ~93% (Fig. 8b). However, for a relatively high LED of 20 kJ/m, the maximum relative density decreases to ~92% and the minimum is ~90% in the bottom of the melt pool (Fig. 8c), due to the insufficiency of gas removal from the melt pool (Fig. 7c). As LED further increases to 22.5 kJ/m, the relative density further decreases to ~90% in the whole melt pool. In comparison with the previous three cases, the areas of the minimum density appear in the middle regions of the metal pool (Fig. 8d), other than in the bottom of the pool (Fig. 8a–c).

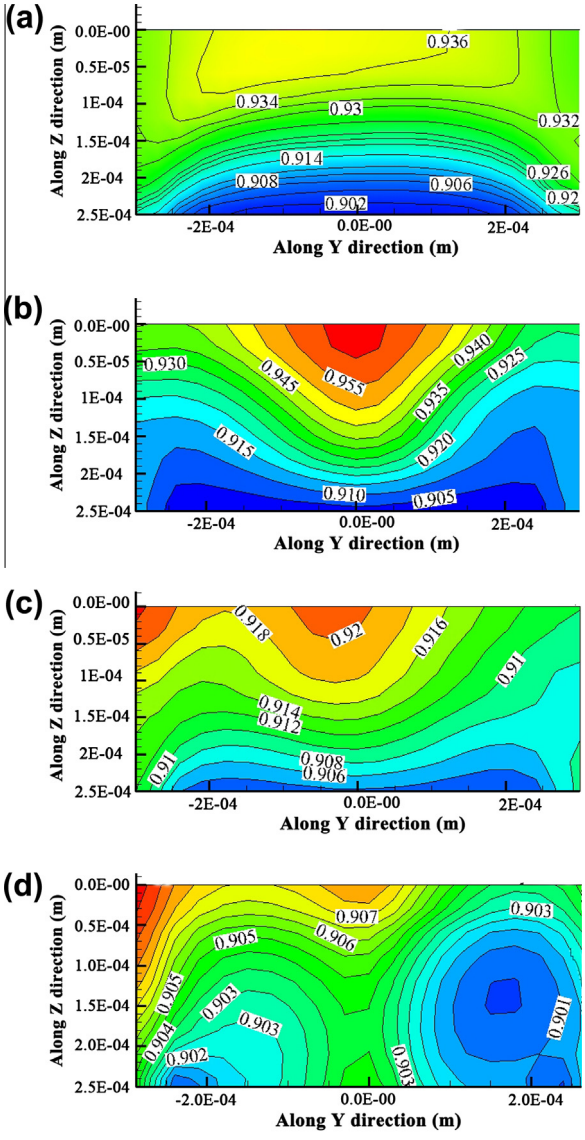

Fig. 8. The relative density contour plots of the melt pool at various LEDs (cross-sectional view): (a) LED = 15 kJ/m, (b) LED = 17.5 kJ/m, (c) LED = 20 kJ/m, and (d) LED = 22.5 kJ/m.

At a relatively low LED of 15 kJ/m, a lower operative temperature (Fig. 3a) and attendant higher melt viscosity, μ, are obtained in the melt pool. As a result, the gaseous bubbles float up in a lower speed (Fig. 5). It is rather difficult for the bubbles to escape from the melt pool, which subsequently induces a lower density (Fig. 8a). As LED increases to 17.5 kJ/m, the significantly decreased viscosity contributes to the formation of lower viscous drag forces, leading to an elevated speed of bubbles. Therefore, the gaseous bubbles escape from the melt pool easily, thus achieving a higher SLM densification (Fig. 8b). With a further enhancement of LED above 20 kJ/m, the sharply reduced surface tension (σ) in the melt pool can be the propulsion for the formation of a higher Eötvös number (E_o), which is regarded as proportional to buoyancy force induced by surface tension force, as revealed by Refs. [43,44]. In this situation, the gaseous bubbles tend to undergo the significant deformation and, accordingly, break into bubbles with smaller radii, which exist in the whole region with the decreased speeds (Figs. 5 and 8c and d). Thereafter, bubbles are easily trapped in the melt pool, resulting in the formation of the reduced density (Fig. 8c and d). Furthermore, there is also a position variation in porosity along *Y*-axis. The densification level in the center is higher than that in the boundary area. It is known that the solidification of the molten pool firstly begins at edges because of (i) the lower operative temperature than that in the center and (ii) the faster heat loss through conductivity after removing the laser beam [45,46]. Consequently, the bubbles at the edges of the molten pool are not easy to escape from the pool and remained as the porosity in the solidified materials, resulting in a lower densification level at the edges of the solidified pool.

4.5. Experiment verification

The cross-sections of SLM-processed WC/Cu powder system under different LEDs are depicted in Fig. 9. At a relative low LED of 15 kJ/m, a large amount of bubbles are entrapped within the melt pool and the irregular pores are present after SLM, with the average size of 200 μm (Fig. 9a). As the applied LED increases to 17.5 kJ/m, a small amount of residual pores in the solidified melt pool reduce their average size to 50 μm (Fig. 9b). However, for a relatively high LED of 20 kJ/m, bubbles have a tendency to be entrapped and remained in the melt pool, accordingly resulting in the formation of pores with the larger size of 300 μm (Fig. 9c). As LED further increases to 22.5 kJ/m, clusters of pores are found in the solidified melt pool due to the appearance of the larger scaled vortex (Fig. 6d), thereby resulting in the aggregation of pores (Fig. 9d). Fig. 10 shows the comparison of relative densities calculated by numerical simulation with those obtained by experiments at different LEDs. The quantitative measurement shows that the relative densities obtained by simulation have a good accordance with those acquired by experiments. For instance, at the LED of 17.5 kJ/m, the average relative density by simulation is 95% and the result measured by experiments is (94 ± 2)%. Therefore, a close look at the experiment and simulation results reveals that the formation and development behaviors of pores are in a good agreement with the simulation results.

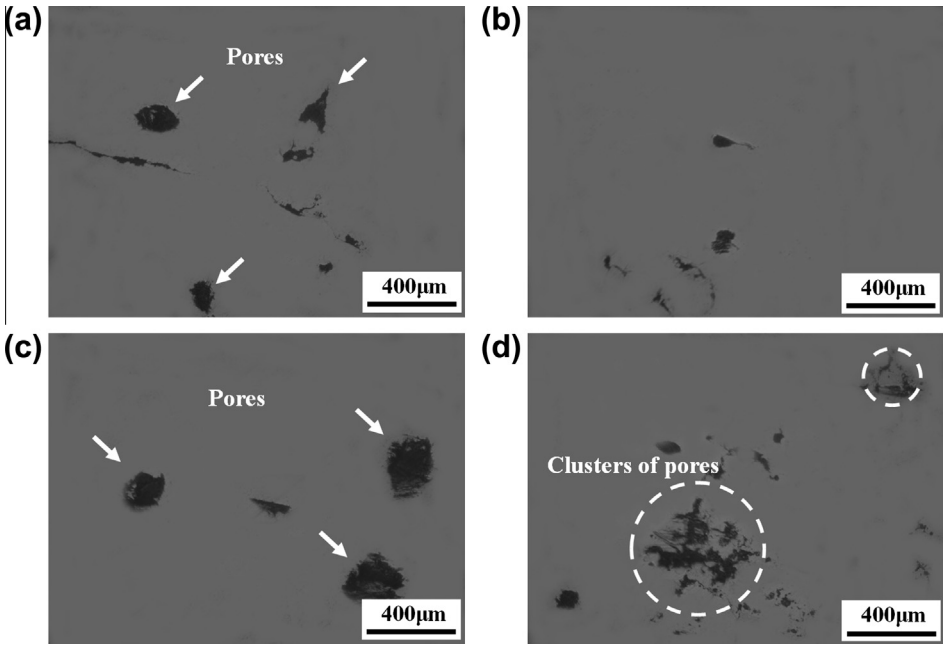

Fig. 9. OM micrographs of SLM-processed WC/Cu samples at different LEDs (cross-sectional view): (a) LED = 15 kJ/m, (b) LED = 17.5 kJ/m, (c) LED = 20 kJ/m, and (d) LED = 22.5 kJ/m.

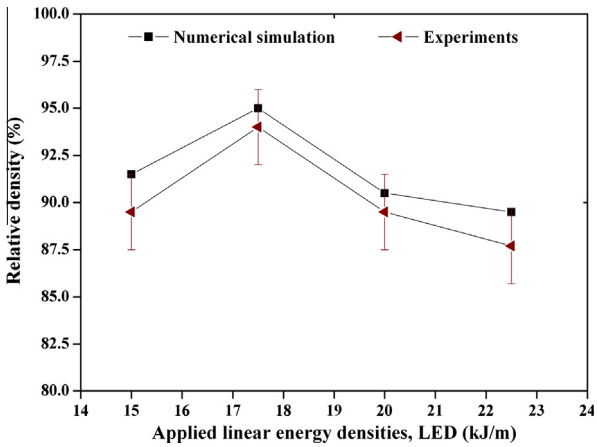

Fig. 10. Comparison of relative densities calculated by numerical simulation with the results obtained by experiments at different LEDs.

5. Conclusions

The simulation of temperature distribution and densification process of selective laser melting (SLM) WC/Cu composite powder system has been performed, using a finite volume method (FVM), and the following conclusions can be drawn.

(1) The temperature increases with the input LEDs and the temperature filed curves are asymmetric. The center of the melt pool does not locate at the center of the laser beam, but slightly shifts towards the side of the decreasing *X*-axis. This phenomenon is induced by the thermal accumulation effect and the thermal conductivity change because of the transition from powder to solid.

(2) The three-dimensions of the melt pool are in sizes of hundreds of micrometers and increase with the applied LEDs. The melt pool length is typically larger than the width and depth of the pool.

(3) The applied LEDs play a crucial role in determining the relative density of SLM-processed parts. For an optimized LED of 17.5 kJ/m, an increased efficiency of gas removal from the melt pool is realized, and the obtained maximum relative density is 96%. However, as the applied LED increases to 22.5 kJ/m, the relative density decreases sharply and the high porosity appears in the middle region of the melt pool.

(4) As the applied LED surpasses 20 kJ/m, Marangoni flow tends to retain the entrapped gas bubbles. The flow pattern has a tendency to deposit the gas bubbles at the melt pool bottom or to agglomerate gas bubbles by the rotating flow in the melt pool, resulting in a higher porosity in SLM-processed powder.

(5) The relative density and corresponding pore size and morphologies are experimentally acquired, which are in a good agreement with the results predicted by simulation.

Acknowledgments

The financial support from the National Nature Science Foundation of China (Nos. 51104090 and 51322509), the Outstanding Youth Foundation of Jiangsu Province of China (No. BK20130035), and the NUAA Fundamental Research Funds (No. NE2013103) is gratefully appreciated.

References

[1] Yusoff M, Othman R, Hussain Z. Mechanical alloying and sintering of nanostructured tungsten carbide-reinforced copper composite and its characterization. Mater Des 2011;32:3293–8.
[2] Deshpande PK, Li JH, Lin RY. Infrared processed Cu composites reinforced with WC particles. Mater Sci Eng A 2006;429:58–65.
[3] Gu DD, Shen YF. Direct laser sintered WC–10Co/Cu nanocomposites. Appl Surf Sci 2008;254:3971–8.
[4] Barrena MI, Gómez de Salazar JM, Matesanz L. Interfacial microstructure and mechanical strength of WC–Co/90MnCrV8 cold work tool steel diffusion bonded joint with Cu/Ni electroplated interlayer. Mater Des 2010;31:3389–94.
[5] Slipenyuk A, Kuprin V, Milman Y, Spowart JE, Miracle DB. The effect of matrix to reinforcement particle size ratio (PSR) on the microstructure and mechanical properties of a P/M processed AlCuMn/SiCp MMC. Mater Sci Eng A 2004;381:165–70.

[6] Zhang BC, Fenineche NE, Liao HL, Coddet C. Microstructure and magnetic properties of Fe–Ni alloy fabricated by selective laser melting Fe/Ni mixed powders. J Mater Sci Technol 2013;29:757–60.
[7] Li RD, Shi YS, Liu JH, Xie Z, Wang ZG. Selective laser melting W–10 wt% Cu composite powders. Int J Adv Manuf Technol 2010;48:597–605.
[8] Gu DD, Hagedorn YC, Meiners W, Meng GB, Batista RJS, Wissenbach K, et al. Densification behavior, microstructure evolution, and wear performance of selective laser melting processed commercially pure titanium. Acta Mater 2012;60:3849–60.
[9] Song B, Dong SJ, Zhang BC, Liao HL, Coddet C. Effects of processing parameters on microstructure and mechanical property of selective laser melted Ti6Al4V. Mater Des 2012;35:120–5.
[10] Sun JF, Yang YQ, Wang D. Mechanical properties of a Ti6Al4V porous structure produced by selective laser melting. Mater Des 2013;49:545–52.
[11] King D, Tansey T. Alternative materials for rapid tooling. J Mater Process Technol 2002;121:313–7.
[12] Zhang BC, Fenineche NE, Zhu L, Liao HL, Coddet C. Studies of magnetic properties of permalloy (Fe–30% Ni) prepared by SLM technology. J Magn Magn Mater 2012;324:495–500.
[13] Gu DD, Shen YF. Balling phenomena in direct laser sintering of stainless steel powder: metallurgical mechanisms and control methods. Mater Des 2009;30:2903–10.
[14] Simchi A. Direct laser sintering of metal powders: mechanism, kinetics and microstructural features. Mater Sci Eng A 2006;428:148–58.
[15] Kruth JP, Levy G, Klocke F, Childs THC. Consolidation phenomena in laser and powder-bed based layered manufacturing. CIRP Ann-Manuf Technol 2007;56:730–59.
[16] Dadbakhsh S, Hao L, Sewell N. Effect of selective laser melting layout on the quality of stainless steel parts. Rapid Prototyping J 2012;18:241–9.
[17] Brandl E, Heckenberger U, Holzinger V, Buchbinder D. Additive manufactured AlSi10Mg samples using selective laser melting (SLM): microstructure, high cycle fatigue, and fracture behavior. Mater Des 2012;34:159–69.
[18] Zhang BC, Liao HL, Coddet C. Effects of processing parameters on properties of selective laser melting Mg–9% Al powder mixture. Mater Des 2012;34:753–8.
[19] Hazlehurst K, Wang CJ, Stanford M. Evaluation of the stiffness characteristics of square pore CoCrMo cellular structures manufactured using laser melting technology for potential orthopaedic applications. Mater Des 2013;51:949–55.
[20] Ghosh SK, Saha P. Crack and wear behavior of SiC particulate reinforced aluminium based metal matrix composite fabricated by direct metal laser sintering process. Mater Des 2011;32:139–45.
[21] Ferrar B, Mullen L, Jones E, Stamp R, Sutcliffe CJ. Gas flow effects on selective laser melting (SLM) manufacturing performance. J Mater Process Technol 2012;212:355–64.
[22] Simchi A, Pohl H. Effects of laser sintering processing parameters on the microstructure and densification of iron powder. Mater Sci Eng A 2003;359:119–28.
[23] Zhang BC, Liao H, Coddet C. Selective laser melting commercially pure Ti under vacuum. Vacuum 2013;95:25–9.
[24] Dong WC, Lu SP, Li DZ, Li YY. Numerical simulation of effects of the minor active-element oxygen on the Marangoni convection and the weld shape. Acta Metall Sin 2008;44:249–56.
[25] Alhendal Y, Turan A, Aly WIA. VOF simulation of Marangoni flow of gas bubbles in 2D-axisymmetric column. Procedia Comput Sci 2010;1:673–80.
[26] Lörstad D, Fuchs L. High-order surface tension VOF-model for 3D bubble flows with high density ratio. J Comput Phys 2004;200:153–76.
[27] Xiao B, Zhang YW. Marangoni and buoyancy effects on direct metal laser sintering with a moving laser beam. Numer Heat Tra-Appl 2007;51:715–33.
[28] Yang J, Wang F. 3D finite element temperature field modelling for direct laser fabrication. Int J Adv Manuf Technol 2009;43:1060–8.
[29] Dai K, Shaw L. Thermal and mechanical finite element modeling of laser forming from metal and ceramic powders. Acta Mater 2004;52:69–80.
[30] Reeber RR, Wang K. Thermophysical properties of α-tungsten carbide. J Am Ceram Soc 1999;82:129–35.
[31] Zhang J, Li DY, Li JY, Zhao LZ. Numerical simulation of temperature field in selective laser sintering. Computer and computing technologies in agriculture IV, 347. Berlin, Heidelberg: Springer; 2011.
[32] Gu DD, Meng GB, Hong C. Densification, microstructure, and wear property of in situ titanium nitride-reinforced titanium silicide matrix composites prepared by a novel selective laser melting process. Metall Mater Trans A 2012;43:697–708.
[33] Gu DD, Meiners W, Wissenbach K, Poprawe R. Laser additive manufacturing of metallic components: materials, processes and mechanisms. Int Mater Rev 2012;57:133–64.
[34] Mumtaz KA, Erasenthiran P, Hopkinson N. High density selective laser melting of Waspaloy®. J Mater Process Technol 2008;195:77–87.
[35] Zhang BC, Liao HL, Coddet C. Microstructure evolution and density behavior of CP Ti parts elaborated by self-developed vacuum selective laser melting system. Appl Surf Sci 2013;279:310–6.
[36] Song B, Dong SJ, Liu Q, Liao HL, Coddet C. Vacuum heat treatment of iron parts produced by selective laser melting: microstructure, residual stress and tensile behavior. Mater Des 2014;54:727–33.
[37] Hussein A, Hao L, Yan C, Everson R. Finite element simulation of the temperature and stress fields in single layers built without-support in selective laser melting. Mater Des 2013;52:638–47.
[38] Song B, Dong SJ, Coddet P, Liao HL, Coddet C. Fabrication of NiCr alloy parts by selective laser melting: columnar microstructure and anisotropic mechanical behavior. Mater Des 2014;53:1–7.
[39] Guan YC, Zhou W, Li ZL, Zheng HY. Influence of overlapping tracks on microstructure evolution and corrosion behavior in laser-melt magnesium alloy. Mater Des 2013;52:452–8.
[40] Tsotridis G, Rother H, Hondros ED. Marangoni flow and the shapes of laser-melted pools. Naturwissenschaften 1989;76:216–8.
[41] Zhang YW, Faghri A. Analysis of forced convection heat transfer in microencapsulated phase change material suspensions. J Thermophys Heat Transfer 1995;9:727–32.
[42] Gu DD, Shen YF, Lu ZJ. Microstructural characteristics and formation mechanism of direct laser-sintered Cu-based alloys reinforced with Ni particles. Mater Des 2009;30:2099–107.
[43] Dai GC, Chen MH. Chemical engineering fluid mechanics. Beijing: Chemical Industry Press; 1988.
[44] Drenchev L, Sobczak J, Asthana R, Malinov S. Mathematical modelling and numerical simulation of ordered porosity metal materials formation. J Comput Aided Mater Des 2003;10:35–54.
[45] Li CW, Wang Y, Zhan HX, Han T, Han B, Zhao WM. Three-dimensional finite element analysis of temperatures and stresses in wide-band laser surface melting processing. Mater Des 2010;31:3366–73.
[46] Han GM, Zhao J, L JQ. Dynamic simulation of the temperature field of stainless steel laser welding. Mater Des 2007;28:240–5.